Catadioptric Camera Calibration Using Geometric Invariants

Xianghua Ying and Zhanyi Hu

Abstract—Central catadioptric cameras are imaging devices that use mirrors to enhance the field of view while preserving a single effective viewpoint. In this paper, we propose a novel method for the calibration of central catadioptric cameras using geometric invariants. Lines and spheres in space are all projected into conics in the catadioptric image plane. We prove that the projection of a line can provide three invariants whereas the projection of a sphere can only provide two. From these invariants, constraint equations for the intrinsic parameters of catadioptric camera are derived. Therefore, there are two kinds of variants of this novel method. The first one uses projections of lines and the second one uses projections of spheres. In general, the projections of two lines or three spheres are sufficient to achieve catadioptric camera calibration. One important conclusion in this paper is that the method based on projections of spheres is more robust and has higher accuracy than that based on projections of lines. The performances of our method are demonstrated by both the results of simulations and experiments with real images.

Index Terms—Camera calibration, catadioptric camera, geometric invariant, omnidirectional vision, panoramic vision.

1 Introduction

In many computer vision applications, including robot navigation, virtual reality, surveillance, teleconferencing, and image-based rendering, a camera with a quite large field of view is required. A conventional camera has a very limited field of view. One effective way to enhance the field of view of a camera is to combine the camera with mirrors. There are some representative implementations of catadioptric imaging systems described in [5], [15], [17], [24], [27]. Recently, Baker and Nayar [2] investigate these catadioptric systems with respect to a single viewpoint constraint. Catadioptric systems can be classified into two classes, central and noncentral, depending on whether they have a single viewpoint or not [2], [10], [19]. A single viewpoint is highly desirable because it allows generating perspective images from the images captured by a central catadioptric camera as if it were taken with a perspective camera whose projection center is located at the effective viewpoint. This paper aims at the calibration of central catadioptric cameras.

Here is a brief review of the methods proposed by others for the central catadioptric camera calibration.

1. **Known World Coordinates**. This kind of methods uses a calibration pattern with control points whose 3D world coordinates are known. These control points can be corners, dots, or any features that can be easily extracted from images. Using iterative methods, the extrinsic parameters (position and orientation) and the intrinsic parameters can be recovered [1], [14], [26]. Note that these calibration techniques can be used for both central and noncentral catadioptric cameras.
2. **Self-calibration**. This kind of calibration techniques uses only point correspondences in multiple views, without needing to know either the 3D locations of space points or the camera locations. Kang [16] uses the consistency of pairwise tracked point features across a sequence to develop a reliable calibration method for a paracatadioptric camera. Geyer and Daniilidis [12] propose a novel 4×4 catadioptric fundamental matrix for paracatadioptric camera and prove that the image of the absolute conic belongs to the kernel of this matrix.
3. **Projections of lines**. This kind of methods uses only the images of lines in the scene, without knowledge of any metric information. Geyer and Daniilidis [10] use images of two sets of parallel lines to find the intrinsic parameters as well as the orientation of the plane containing the two parallel line sets. Barreto and Araújo [3] present a two-step method: First, the principal point is determined using the intersections of three catadioptric line images. Second, the recovered principal point is used to determine the image of the absolute conic from these line images. More recently, Geyer and Daniilidis [13] propose another calibration method for a paracatadioptric camera using the projective properties of the images of three lines.

In this paper, we propose a novel calibration method based on geometric invariants, which provides a unified framework for the calibration using either images of lines or images of spheres. The motivations for proposing this novel method are based on the following facts:

1. Lines and spheres are two common geometric entities in real scenes, and they are often used for

• *The authors are with the National Laboratory of Pattern Recognition, Institute of Automation, Chinese Academy of Sciences, PO Box 2728, Beijing, P.R. China, 100080. E-mail: {xhying, huzy}@nlpr.ia.ac.cn.*

Manuscript received 7 Oct. 2003; revised 24 Feb. 2004; accepted 9 Mar. 2004. Recommended for acceptance by L. Quan.
For information on obtaining reprints of this article, please send e-mail to: tpami@computer.org, and reference IEEECS Log Number TPAMI-0308-1003.

the conventional camera calibration [6], [7], [20], [23], [25]. It is well known that, under central catadioptric cameras, a line in space is projected into a conic in the image plane [18], [24]. We further prove that the projected occluding contour of a sphere in space is also a conic in the catadioptric image plane. Based on this fact, we present a unified framework to cover both the projections of lines and those of spheres.

2. Using the unified framework, we prove that, in general, the projection of a space line can provide three invariants whereas the projection of a space sphere can only provide two when the 3D locations of the line and the sphere are unknown. From these invariants, the constraint equations for the intrinsic parameters can be derived. Therefore, the projections of either two lines or three spheres are sufficient to achieve the catadioptric camera calibration (note that Geyer and Daniilidis [11] only discuss the number of constraints provided by a line image, but no actual constraint equations are given). Different from the methods proposed in [3], [10] which must use the intersections of line images to determine the principle point in the first step, our method directly uses the constraint equations provided by a single-line or a single-sphere image. One advantage of our method is that we can perform the calibration in the case where the minimum number of line or sphere images is available. Another advantage of our method is that in the case where the number of line or sphere images is not sufficient for full intrinsic parameter calibration (e.g., only one line image is available), the calibration can also be done partially. We further prove that the method proposed in [13] is a special case within our unified framework.
3. One important contribution of this paper is to introduce spheres as calibration features for the central catadioptric camera calibration. Although lines and spheres are all projected into conics in the image plane, it is more difficult to extract the projection of a line with high accuracy than that of a sphere. The main underlying reason is that, the projection of a line (usually a line segment in real scene) is only a small arc of a conic (e.g., about one-third of an ellipse) but the projection of a sphere is usually a closed ellipse, and conic fitting using points lying on a portion of a conic is an error-prone process. As we know, the accuracy of the estimated intrinsic parameters highly depends on the accuracy of the extracted conics. Therefore, sphere images are preferred in the case where accurate calibration of central catadioptric cameras is needed.

This paper is organized as follows: Section 2 briefly introduces a generalized image formation model for central catadioptric cameras. In Section 3, the invariants and the constraint equations on the intrinsic parameters provided by line images and sphere images are derived. Section 4 describes a novel efficient two-stage calibration technique. Experimental results are shown in Section 5. Finally, Section 6 presents some concluding remarks.

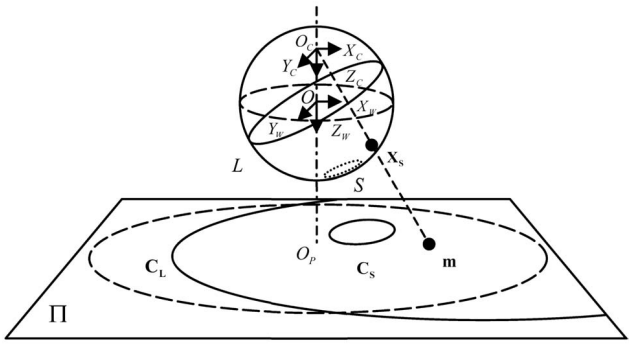

Fig. 1. The generalized image formations of a point (as illustrated in Section 2), a line, and a sphere (as illustrated in Section 3) in space are shown, respectively. A space point is projected to point $\mathbf{X_S}$ on the viewing sphere, then projected to $\mathbf{m}$ on the image plane Π from O_C. A sphere in space is projected to a small circle S on the viewing sphere, then projected to a conic section $\mathbf{C_S}$ on the image plane from O_C. A line in space is projected to a great circle L on the viewing sphere, then projected to a conic section $\mathbf{C_L}$ on the image plane. The equator of the viewing sphere is mapped to the dashed circle on the image plane.

2 A Generalized Image Formation Model for Central Catadioptric Cameras

Baker and Nayar [2] show that the only useful physically realizable mirror surfaces of catadioptric cameras that produce a single viewpoint are planar, ellipsoidal, hyperboloidal, and paraboloidal. Recently, Geyer and Daniilidis [11] propose a generalized image formation model for these central catadioptric cameras. They prove that the central catadioptric image formation is equivalent to a two-step mapping via a sphere:

Step 1. A point in 3D space is projected to a point on a unit sphere centered at the single effective viewpoint. The unit sphere is called the viewing sphere. Considering a general 3D space point, visible by a catadioptric camera, with Cartesian coordinates $\mathbf{X} = (X_W \;\; Y_W \;\; Z_W)^T$ in the world coordinate system whose origin is at the single viewpoint, the projection of $\mathbf{X}$ on the viewing sphere is:

$$\mathbf{X_S} = (X_S \;\; Y_S \;\; Z_S)^T = \left(\frac{X_W}{\sqrt{X_W^2 + Y_W^2 + Z_W^2}} \; \frac{Y_W}{\sqrt{X_W^2 + Y_W^2 + Z_W^2}} \; \frac{Z_W}{\sqrt{X_W^2 + Y_W^2 + Z_W^2}} \right)^T. \quad (1)$$

Step 2. The point $\mathbf{X_S}$ on the viewing sphere is perspectively projected to a point $\mathbf{m}$ on the image plane Π from another point O_C. The image plane Π is perpendicular to the line determined by the single viewpoint O and O_C (see Fig. 1).

This step can be considered as taking image of the viewing sphere using a virtual camera whose optical center is located at O_C and whose optical axis coincides with the line determined by O and O_C. Once the intrinsic parameters of the virtual camera are estimated, the intrinsic parameters of the central catadioptric camera are known. In general, we distinguish five intrinsic parameters for the virtual camera: the principal point $O_P\,(u_0, v_0)$, the effective focal length

TABLE 1
Eccentricity ε and Distance l

	Ellipsoidal	Paraboloidal	Hyperboloidal	Planar
ε	$0<\varepsilon<1$	$\varepsilon=1$	$\varepsilon>1$	$\varepsilon\to\infty$
l	$0<l<1$	$l=1$	$0<l<1$	$l=0$

$f_e = |O_C O_P|$, the aspect ratio r and the skew factor s. The intrinsic matrix of the virtual camera can be written as:

$$\mathbf{K} = \begin{bmatrix} r\cdot f_e & s & u_0 \\ 0 & f_e & v_0 \\ 0 & 0 & 1 \end{bmatrix}. \tag{2}$$

The distance, $l = |OO_C|$, can be regarded as another parameter of the catadioptric camera. Therefore, there are totally six parameters required to be calibrated. The projection of $\mathbf{X_S}$, i.e., $\mathbf{m} = (\,x \quad y \quad 1\,)^T$ on the catadioptric image plane Π, satisfies:

$$\lambda\mathbf{m} = \mathbf{K}\begin{bmatrix} 1 & 0 & 0 & 0 \\ 0 & 1 & 0 & 0 \\ 0 & 0 & 1 & l \end{bmatrix}\begin{bmatrix} X_S \\ Y_S \\ Z_S \\ 1 \end{bmatrix}, \tag{3}$$

where λ is an unknown scalar factor. For a catadioptric camera with a mirror whose surface is a conic section surface of revolution, it satisfies [11]:

$$l = \frac{2\varepsilon}{1+\varepsilon^2}, \tag{4}$$

where ε is the eccentricity of the conic section. The relationship between ε and l for different types of central catadioptric cameras is shown in Table 1.

3 Invariants of Line and Sphere Images

In this section, first, the equations of line and sphere images from a catadioptric camera are derived under a unified framework. Second, the invariants are obtained from the geometric properties of the metric catadioptric projections of lines and spheres. Finally, the constraint equations for the intrinsic parameters are derived from these invariants.

3.1 Equations of Line and Sphere Images

Definition 1. *The metric catadioptric projection is a projection induced by a central catadioptric camera whose intrinsic parameters are as follows: $r = 1$, $s = 0$, $u_0 = 0$, and $v_0 = 0$. Correspondingly, the projection induced by a central catadioptric camera whose intrinsic matrix is defined by (2) is called the generic catadioptric projection.*

We first derive the equations of line and sphere images under metric catadioptric projection, and then derive the equations under generic catadioptric projection. For the case of metric catadioptric projection, the camera intrinsic matrix can be rewritten as:

$$\mathbf{K_M} = \begin{bmatrix} f_e & 0 & 0 \\ 0 & f_e & 0 \\ 0 & 0 & 1 \end{bmatrix}. \tag{5}$$

Under metric catadioptric projection, the origin of the image coordinate system is located at the principal point, and the geometric properties of the projections of lines and spheres can be easily discovered. These geometric properties are described as invariants in Section 3.2.

The generalized image formations of a line and a sphere in space are shown in Fig. 1. It is well known that a line in space is projected to a great circle whereas the projected occluding contour of a sphere in space is a small circle on the viewing sphere. We know that the intersection curve of a plane and a sphere is a circle. The plane is called the base plane related to the circle. If the base plane passes through the spherical center, the circle is a great circle. Otherwise the circle is a small circle. Assume a small circle, the projected occluding contour of a sphere on the viewing sphere, lies on a base plane $(n_x\ n_y\ n_z\ d_0)^T$, where $(n_x\ n_y\ n_z)^T$ is the unit normal vector for the base plane, and $|d_0|$ is the distance from the origin O to the base plane, then a point $(X_S\ Y_S\ Z_S)^T$ on the small circle satisfies:

$$\begin{cases} n_x X_S + n_y Y_S + n_z Z_S + d_0 = 0 \\ X_S^2 + Y_S^2 + Z_S^2 = 1 \end{cases}. \tag{6}$$

Similarly, a great circle, the image of a line on the viewing sphere, lies on a base plane $(n_x\ n_y\ n_z\ 0)^T$ passing through the origin O, then a point $(X_S\ Y_S\ Z_S)^T$ on the great circle satisfies:

$$\begin{cases} n_x X_S + n_y Y_S + n_z Z_S = 0 \\ X_S^2 + Y_S^2 + Z_S^2 = 1 \end{cases}. \tag{7}$$

Obviously, a great circle is a special case of a small circle when the distance from the origin to the base plane is zero (i.e., by setting $d_0 = 0$ in (6), we can obtain (7)). Therefore, there exists a unified framework to represent the projections of a line and a sphere on the viewing sphere. Consequently, the equations for a sphere derived from (6) can be changed into the equations for a line by setting $d_0 = 0$. Substituting (5) into (3), we get:

$$\lambda\mathbf{m} = \lambda\begin{bmatrix} x \\ y \\ 1 \end{bmatrix} = \begin{bmatrix} f_e & 0 & 0 \\ 0 & f_e & 0 \\ 0 & 0 & 1 \end{bmatrix}\begin{bmatrix} 1 & 0 & 0 & 0 \\ 0 & 1 & 0 & 0 \\ 0 & 0 & 1 & l \end{bmatrix}\begin{bmatrix} X_S \\ Y_S \\ Z_S \\ 1 \end{bmatrix}. \tag{8}$$

Eliminating X_S, Y_S, Z_S, and λ from (6) and (8), and rewriting in matrix form, we obtain the quadratic form for the metric catadioptric projection of a space sphere is:

$$\mathbf{C_S} = \begin{bmatrix} (l^2-1)n_x^2+(d_0-l\cdot n_z)^2 & (l^2-1)n_x n_y & (ld_0-n_z)f_e n_x \\ (l^2-1)n_x n_y & (l^2-1)n_y^2+(d_0-l\cdot n_z)^2 & (ld_0-n_z)f_e n_y \\ (ld_0-n_z)f_e n_x & (ld_0-n_z)f_e n_y & f_e^2(d_0^2-n_z^2) \end{bmatrix}. \tag{9}$$

By setting $d_0 = 0$ in (9), we obtain the quadratic form for the metric catadioptric projection of a space line:

$$\mathbf{C_L} = \begin{bmatrix} (l^2-1)n_x^2 + l^2 n_z^2 & (l^2-1)n_x n_y & -f_e n_z n_x \\ (l^2-1)n_x n_y & (l^2-1)n_y^2 + l^2 n_z^2 & -f_e n_z n_y \\ -f_e n_z n_x & -f_e n_z n_y & -f_e^2 n_z^2 \end{bmatrix}. \tag{10}$$

It is not difficult to prove that (10) is equivalent to the equation for a line image derived in [11], but (10) has a more concise form.

In order to derive the equations under generic catadioptric projection, we decompose the camera intrinsic matrix $\mathbf{K}$ defined by (2) into the product of two matrices:

$$\mathbf{K} = \mathbf{K_A}\mathbf{K_M}, \tag{11}$$

where

$$\mathbf{K_A} = \begin{bmatrix} r & s' & u_0 \\ 0 & 1 & v_0 \\ 0 & 0 & 1 \end{bmatrix} \tag{12}$$

and $s' = s/f_e$. The matrix $\mathbf{K_M}$ is defined by (5).

Under metric catadioptric projection, i.e., where the camera intrinsic matrix is equal to $\mathbf{K_M}$, the equation of an image conic (a projection of a line or a sphere) can be written as:

$$\mathbf{m}^T\mathbf{C}\mathbf{m} = 0, \tag{13}$$

where

$$\mathbf{C} = \begin{bmatrix} a & b & d \\ b & c & e \\ d & e & f \end{bmatrix}, \ \mathbf{m} = \begin{bmatrix} x \\ y \\ 1 \end{bmatrix}.$$

For the case of generic catadioptric projection, i.e., the intrinsic matrix $\mathbf{K}$ defined by (2), the equation of an image conic (a projection of a line or a sphere) is represented as:

$$\mathbf{m'}^T\mathbf{C'}\mathbf{m'} = 0, \tag{14}$$

where

$$\mathbf{C'} = \begin{bmatrix} a' & b' & d' \\ b' & c' & e' \\ d' & e' & f' \end{bmatrix}, \ \mathbf{m'} = \begin{bmatrix} u \\ v \\ 1 \end{bmatrix}.$$

$\mathbf{m}'$ are the pixel coordinates in the image coordinate system. From the definitions of $\mathbf{m}$ and $\mathbf{m}'$, we know $\mathbf{m}' = \mathbf{K_A}\mathbf{m}$. So,

$$\mathbf{C} = \mathbf{K_A}^T\mathbf{C'}\mathbf{K_A}, \tag{15}$$

or

$$\mathbf{C'} = \mathbf{K_A}^{-T}\mathbf{C}\mathbf{K_A}^{-1}. \tag{16}$$

From (9), (10), and (16), we notice that the metric and generic catadioptric projections of a line and a sphere are both conics. Since $\mathbf{K_A}$ is an invertible affine transformation, $\mathbf{C}$ and $\mathbf{C}'$ belong to the same affine classification of conics.

3.2 Invariants of Line and Sphere Images

If a conic

$$\mathbf{C} = \begin{bmatrix} a & b & d \\ b & c & e \\ d & e & f \end{bmatrix}$$

is the metric catadioptric projection of a sphere in space (or a line in space as a special case), we intend to find what constraints the conic must satisfy, and what constraints the conic can provide for l and f_e.

Under metric catadioptric projection, the projection matrix of the virtual camera is:

$$\mathbf{P} = \begin{bmatrix} f_e & 0 & 0 & 0 \\ 0 & f_e & 0 & 0 \\ 0 & 0 & 1 & l \end{bmatrix}.$$

The world coordinate system is established as in Fig. 1. From Proposition 1 in [21], we obtain the cone determined by the conic $\mathbf{C}$ and the projection center of the virtual camera O_C is:

$$\mathbf{Q} = \mathbf{P}^T\mathbf{C}\mathbf{P} = \begin{bmatrix} af_e^2 & bf_e^2 & df_e & dlf_e \\ bf_e^2 & cf_e^2 & ef_e & elf_e \\ df_e & ef_e & f & fl \\ dlf_e & elf_e & fl & fl^2 \end{bmatrix}.$$

The quadric form of the viewing sphere is:

$$\mathbf{V_S} = \begin{bmatrix} 1 & 0 & 0 & 0 \\ 0 & 1 & 0 & 0 \\ 0 & 0 & 1 & 0 \\ 0 & 0 & 0 & -1 \end{bmatrix}.$$

The linear combination of $\mathbf{Q}$ and $\mathbf{V_S}$ is:

$$\mathbf{H} \equiv \mathbf{Q} + \lambda\mathbf{V_S} = \begin{bmatrix} af_e^2 + \lambda & bf_e^2 & df_e & dlf_e \\ bf_e^2 & cf_e^2 + \lambda & ef_e & elf_e \\ df_e & ef_e & f + \lambda & fl \\ dlf_e & elf_e & fl & fl^2 - \lambda \end{bmatrix}. \tag{17}$$

Consider the pencil of two quadric surfaces $\mathbf{Q_1}$ and $\mathbf{Q_2}$, $\mathbf{Q_1} + \lambda\mathbf{Q_2}$ represents a quadric surface which passes through all the common points of $\mathbf{Q_1}$ and $\mathbf{Q_2}$. The intersection curve of two quadric surfaces is generally a quartic curve in space [22]. In our context, the metric catadioptric projection imposes that the cone $\mathbf{Q}$ intersects the viewing sphere $\mathbf{V_S}$ at a circle in space (a small circle for a space sphere or a great circle for a space line). So, there should exist a base plane containing the circle. Since a pair of planes (distinct or coincident) can be considered as a degenerate quadric surface of rank 2 or rank 1 [22], the base plane should be one of the pair of planes. Therefore, we are led to examine a special pencil of quadric surfaces which contains a degenerated member of rank 2 or rank 1. From the discussion above, we can represent the metric catadioptric projection constraints as follows:

Proposition 1. *There exists a scalar factor λ which makes $\mathbf{H} \equiv \mathbf{Q} + \lambda\mathbf{V_S}$ with rank 2 or rank 1, where $\mathbf{Q}$ is the proper cone corresponding to the metric catadioptric projection conic $\mathbf{C}$, and $\mathbf{V_S}$ is the viewing sphere.*

From the definition of the rank of a matrix, we know, the rank is less than or equal to 2, if and only if all 3×3 submatrices of the matrix are singular. Obviously, the rank of $\mathbf{H} \equiv \mathbf{Q} + \lambda\mathbf{V_S}$ cannot equal 0. Hence, $\mathbf{H}$ with rank 2 or rank 1 is equivalent to all 3×3 submatrices of $\mathbf{H}$ are singular. Because of the symmetry of $\mathbf{H}$, there are totally 10 equations from the singularity of these submatrices. From these equations, after eliminating λ, we can obtain two equations for a, b, c, d, e, f, f_e, l, which are described as:

Proposition 2. *Under metric catadioptric projection, if the image of a sphere in space is*

$$\mathbf{C_S} = \begin{bmatrix} a & b & d \\ b & c & e \\ d & e & f \end{bmatrix},$$

there exist two invariants:
Invariant 1. $S_1 = d(bd - ae) - e(be - cd) = 0.$
Invariant 2. $S_2 = b(bd - ae)f_e^2 - e(bf - de)(l^2 - 1) = 0.$

Since the projection of a line is a great circle on the viewing sphere and the base plane containing the great circle must pass through the origin, there is no constant term in the equation of the base plane. Since $\mathbf{H}$ is reducible, and one of its factors is the equation of the base plane, $\mathbf{H}$ cannot contain a constant term, either. From (17), we obtain:

$$fl^2 - \lambda = 0.$$

From the above equation and 10 equations from the singularity of all 3×3 submatrices of $\mathbf{H}$, we obtain:

Proposition 3. *Under metric catadioptric projection, if the image of a line in space is*

$$\mathbf{C_L} = \begin{bmatrix} a & b & d \\ b & c & e \\ d & e & f \end{bmatrix},$$

there exist three invariants:
Invariant 3. $L_1 = d(bd - ae) - e(be - cd) = 0.$
Invariant 4. $L_2 = bf + de(l^2 - 1) = 0.$
Invariant 5. $L_3 = d(bd - ae)f_e^2 + f(bf - de) = 0.$

From $n_x^2 + n_y^2 + n_z^2 = 1$ and (9), (10), we can easily verify that Invariants 1~5 are true. The geometric interpretations of Invariant 1 and Invariant 3 are that one of major axes of the image conic passes through the origin of the image plane. This property has been discovered by many researchers [7], [11]. For a central conic, Invariants 1 and 3 are equivalent to $dc_x - ec_y = 0$, where (c_x, c_y) is the center of the conic [7]. Invariant 5 can be derived from Invariant 4 and Invariant 2. Obviously, Invariants 1~5 do not contain variables n_x, n_y, n_z, and d_0. That means these invariants do not change no matter where lines and spheres are located in 3D space. It is not difficult to prove that Invariants 1 and 3 are rotation and scale invariants, and Invariants 2, 4, and 5 are rotation invariants. The independency of Invariants 1 and 2 is obvious since Invariant 2 contains parameters f_e and l but Invariant 1 does not. It is the similar reason for the independency of Invariants 3, 4, and 5. These invariants will be used to derive the constraint equations for the intrinsic parameters in Section 3.4.

From above, we notice that, in general, a line image can provide three invariants (constraints) and a sphere image can provide two. The reason is that a general conic can provide five constraints, the orientation of the base plane containing the great circle corresponding to the space line has two unknowns ($n_x, n_y, n_z,$ with $n_x^2 + n_y^2 + n_z^2 = 1$), and the base plane containing the small circle corresponding to the space sphere has three unknowns (d_0 and $n_x, n_y, n_z,$ with $n_x^2 + n_y^2 + n_z^2 = 1$). In the next section, we will discuss the invariants provided by the images of lines and spheres in the degenerated cases.

3.3 Singularities of Invariants

We describe here the singularities of invariants from the images of lines and spheres. Due to lack of space, we are only able to give a sketch of the derivations. A first remark is that singularities occur if and only if the catadioptric image conics of lines and spheres degenerate into lines or circles. A second observation is that for these singular cases there exist necessary and sufficient conditions (see Proposition 4 and Proposition 5).

Proposition 4. *The metric catadioptric image of a line (or a sphere) in space is a circle, if and only if $l = 1$ or $n_z = 1$.*

Proof. The projection conic

$$\mathbf{C} = \begin{bmatrix} a & b & d \\ b & c & e \\ d & e & f \end{bmatrix}$$

is a circle, if and only if $a = c \;\; b = 0$.

Necessary: From $a = c \;\; b = 0$ and (10) (or (9)), we can obtain: $l = 1$ or $n_x = n_y = 0$. Since $n_x^2 + n_y^2 + n_z^2 = 1$, we have $n_z = 1$.

Sufficient: Substituting $l = 1$ or $n_z = 1$ into (10) (or (9)), we can obtain $a = c \;\; b = 0$. □

Proposition 5. *The metric catadioptric image of a line in space is a line, if and only if $l = 0$ or $n_z = 0$, and the metric catadioptric image of a sphere in space is a line, if and only if $l \cdot n_z = d_0$.*

Proof. The metric catadioptric image of a line (or a sphere) in space is a line, if and only if the base plane corresponding to the line (or the sphere) passes through the projection center of the virtual camera O_C. The world coordinates of O_C is $(0, 0, -l)^T$. The equation of the base plane corresponding to the sphere is $n_x X + n_y Y + n_z Z + d_0 = 0$. So, the base plane passes through O_C, if and only if $l \cdot n_z = d_0$. By setting $d_0 = 0$, we obtain that the base plane corresponding to the line passes through O_C, if and only if $l \cdot n_z = 0$, i.e., $l = 0$ or $n_z = 0$. □

All singular cases derived from Proposition 4 and Proposition 5 are listed in Table 2. Note that the method in [13] deals with the calibration of a paracatadioptric camera using projections of lines in space corresponds to the singularity Case 1. In this case, a line image is a circle, and gives rise to three invariants. The two of them are:

$$a = c \quad b = 0. \tag{18}$$

Substituting $b = 0$ and $l = 1$ into Invariant 5, we obtain the third one:

$$f_e^2 = -\frac{f}{a}. \tag{19}$$

From (19), we can derive Proposition 1 in [13] which is a key proposition in that paper. The derivation is given in the Appendix.

For Case 3 and Case 4, the centers of these image circles are all located at the origin of the image plane, then we obtain:

$$\begin{matrix} a = c & b = 0 \\ d = 0 & e = 0 \end{matrix}. \tag{20}$$

TABLE 2
Singularities of Invariants from the Images of Lines and Spheres

Case	Conditions		Image	Invariants
1	$l=1$	PLS	Circle	(18), (19)
2		PSS		(18)
3	$n_z=1$	PLS		(20), (21)
4		PSS		(20)
5	$l=0$	PLS	Line	-
6	$n_z=0$	PLS		-
7	$l\cdot n_z=d_0$	PSS		-

"-" means if the image conics degenerate into lines, the corresponding constraints (invariants) will vanish. "PLS" is the abbreviation for "Projection of Line in Space," and "PSS" for "Projection of Sphere in Space."

For Case 3, we can get another invariant:

$$af_e^2+fl^2=0. \tag{21}$$

The case where $l=0$ and the projections of space spheres are used for calibration, is not a singular one since the projection of a sphere is a general conic in this case. A method for the conventional camera calibration using sphere images, proposed in [7], is a special case of our method, since it is well known that the catadioptric camera with a planar mirror is equivalent to a conventional camera. If we substitute $l=0$ into Invariant 2, we obtain:

$$f_e=\sqrt{\frac{e(bf-de)}{b(ae-bd)}}. \tag{22}$$

It is not difficult to verify (22) is equivalent to the formula of the focal length derived in [7].

3.4 Constraints on the Intrinsic Parameters

From (15), we have:

$$\begin{bmatrix} a & b & d\\ b & c & e\\ d & e & f\end{bmatrix}=\begin{bmatrix} r & s' & u_0\\ 0 & 1 & v_0\\ 0 & 0 & 1\end{bmatrix}^T\begin{bmatrix} a' & b' & d'\\ b' & c' & e'\\ d' & e' & f'\end{bmatrix}\begin{bmatrix} r & s' & u_0\\ 0 & 1 & v_0\\ 0 & 0 & 1\end{bmatrix}. \tag{23}$$

Expanding the right side of (23), we obtain:

$$\begin{cases} a=r^2a'\\ b=rs'a'+rb'\\ c=s'^2a'+2s'b'+c'\\ d=ru_0a'+rv_0b'+rd'\\ e=s'u_0a'+u_0b'+s'v_0b'+v_0c'+s'd'+e'\\ f=u_0^2a'+2u_0v_0b'+v_0^2c'+2u_0d'+2v_0e'+f'. \end{cases} \tag{24}$$

Since the image conic $\mathbf{C}'$ can be extracted from the actual catadioptric image using some conic fitting method, the entries of matrix $\mathbf{C}'$ can be known prior to estimating the intrinsic parameters whereas the entries of matrix $\mathbf{C}$ still remain unknown. From the discussions in Section 3.2, we know that, in the nonsingular cases, the entries of matrix $\mathbf{C}$ must satisfy the invariants though these entries are yet unknown. Substituting (24) into Invariants 1 and 2, we obtain two constraint equations on the intrinsic parameters from an image conic of a space sphere. Similarly, substituting (24) into Invariants 3, 4, and 5, we obtain three constraint equations on the intrinsic parameters from an image conic of a space line. There are totally six unknown parameters to be calibrated: five intrinsic parameters and one parameter l. It is sufficient to estimate these parameters if there are six independent constraint equations available. The six constraint equations can be provided by either two line images or three sphere images.

TABLE 3
The Minimum Number of Lines or Spheres for the Calibration of Different Types of Central Catadioptric Cameras

	Planar $l=0$	Hyperboloidal/Ellipsoidal $0<l<1$	Paraboloidal $l=1$
PLS	-	2	3
PSS	3	3	*

The meanings of PLS and PSS are the same as those in Table 2. "-" means calibration cannot be performed, and "" means only r and s' can be recovered.*

For the singular cases presented in Section 3.3, we substitute (24) into the invariants provided by those image conics (see Table 2), then we can obtain the constraint equations on the intrinsic parameters in these cases. Here, we only discuss how to obtain the constraint equations in the singular Case 1. Substituting (24) into (18), we obtain $r^2a'=s'^2a'+2s'b'+c'$ and $rs'a'+rb'=0$. Solving for r,s', we have $r=\sqrt{-\frac{b'^2}{a'^2}+\frac{c'}{a'}}$ and $s'=-\frac{b'}{a'}$. Substituting (24) into (19), we have:

$$\left(-\frac{b'^2}{a'}+c'\right)f_e^2+a'u_0^2+2b'u_0v_0+c'v_0^2+2d'u_0+2e'v_0+f'=0.$$

Since a line image can provide two constraint equations on r,s' and one constraint equation on u_0,v_0,f_e, at least three line images can perform calibration in the singular Case 1.

Table 3 shows the minimum number of line or sphere images needed to achieve the calibration for different types of central catadioptric cameras. We assume these space lines and spheres are all in general position. Note that the minimum number of space lines for calibration have been discussed in [11] when the aspect ratio and the skew factor of the catadioptric camera are known beforehand.

4 Calibration Algorithm

In order to efficiently solve the nonlinear constraint equations on the intrinsic parameters, we present a two-stage calibration technique for the case where the number of line or sphere images is greater than or equal to four in the nonsingular cases.

4.1 Two-Stage Calibration Technique

The two-stage calibration technique is based on the following two observations.

Observation 1. The six constraint equations on the intrinsic parameters provided by two line images or three sphere images are nonlinear. Generally speaking, it is quite hard to solve systems of nonlinear equations.

Observation 2. The constraint equations on the intrinsic parameters derived from Invariants 1 or 3 are only on the parameters r, s', u_0, and v_0, but not on l and f_e. If there

are four or more sphere or line images, we have four or more constraint equations derived from Invariants 1 or 3. Therefore we can use a nonlinear least squares method to solve r, s', u_0, and v_0 provided good initial values of these parameters are available.

Without loss of generality, we only present here the two-stage algorithm based on sphere images, the two-stage algorithm using line images can be constructed in a similar way.

Stage 1. Compute r, s', u_0, and v_0. Given four or more sphere images, derive the constraint equations from Invariant 1 (or its equivalent form, $dc_x - ec_y = 0$), and subsequently use Levenberg-Marquardt algorithm to recover r, s', u_0, and v_0 from these constraint equations. The initial estimations will be discussed in the next section.

Stage 2. Compute l and f_e. Substituting the results of r, s', u_0, and v_0 obtained in the first stage into (23), and then substituting the entries of matrix C obtained from (23) into Invariant 2, we get a quadric equation for the parameters l and f_e. Therefore, in this stage, two sphere images are sufficient to solve for l and f_e using the intersections of the two quadric curves. For a catadioptric camera, the parameter l usually remains constant. If l is known in prior, one sphere image is sufficient to solve for the parameter f_e.

Since the initial guesses of parameters l and f_e are not necessary, we only need to find the initial values of r, s', u_0, and v_0 which will be discussed in the next section.

4.2 Initial Estimations

Similar to [16], the method for finding initial values is to identify the bounding ellipse of the catadioptric image. This can be done by using a predefined threshold, finding the boundary, and fitting an ellipse to the resulting boundary. Note that the boundary is the projection of the mirror boundary, and the mirror boundary is a circle. The plane containing the circle is perpendicular to the optical axis of the camera and the optical axis goes through the center of the circle. It is not difficult to prove that this case is equivalent to the singular Case 4. From Table 2, we know that the image of the boundary can provide four constraints as shown in (20). Substituting (24) into (20), and after some manipulation, the initial values of r, s', u_0, and v_0 can be obtained:

$$\begin{cases} r = \sqrt{-\frac{b'^2}{a'^2} + \frac{c'}{a'}} \\ s' = -\frac{b'}{a'} \\ u_0 = \frac{b'e' - c'd'}{a'c' - b'^2} \\ v_0 = \frac{b'd' - a'e'}{a'c' - b'^2}, \end{cases}$$

where the initial values of (u_0, v_0) is the center of the bounding ellipse.

5 Experiments

We perform a number of experiments with simulated and real data, in order to assess the performances of our calibration algorithm. As we know, the accuracy of the estimated intrinsic parameters highly depends on the accuracy of the extracted conics. In the first experiment, we investigate the qualities of direct least squares fitting of the catadioptric conics of lines and spheres. Then, we compare two variants of our calibration methods: one based on geometric invariants of spheres (**IS**), the other based on geometric invariants of lines (**IL**), with the method based on Properties of Lines (**PL**) proposed in [3] with simulated and real data, respectively. In the real experiments, we use a perspective camera with a hyperbolic mirror, designed by the Center for Machine Perception, Czech Technical University, its field of view (FOV) is 217.2 degree, and the eccentricity of the hyperbolic mirror is $\varepsilon = 1.302$. From (4), we get $l = 0.966$. Here, we assume that the parameter l is known beforehand.

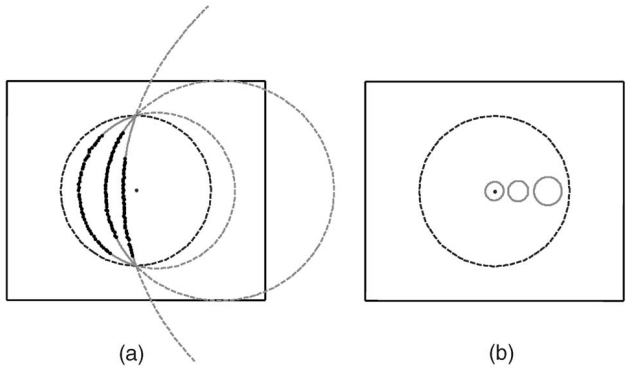

Fig. 2. The catadioptric conics of lines and spheres. (a) Three line images with $\Theta = 0$ and from left to right $\Phi = 15,\ 45,\ \text{and}\ 70$, respectively. (b) Three sphere images with $d_0 = 0.97$, $\Theta = 0$, and from left to right $\Phi = 0, 35,\ \text{and}\ 70$, respectively. The dashed dark circle represents the FOV boundary. The black dots in (a) are the sampled points. Note that, line images undergo the occlusion effects, whereas sphere images do not.

5.1 Catadioptric Conic Fitting

The unit normal vector for the base plane corresponding to a line or a sphere in space can be represented by: $\begin{pmatrix} n_x & n_y & n_z \end{pmatrix}^T = \begin{pmatrix} \sin\Phi\cos\Theta & \sin\Phi\sin\Theta & \cos\Phi \end{pmatrix}^T$, where Φ is the elevation angle and Θ is the azimuth angle in the spherical coordinate system. The value ranges are $\Phi : 0^\circ \sim 180^\circ$ and $\Theta : 0^\circ \sim 360^\circ$, respectively. In this experiment, the FOV of the catadioptric camera is chosen as 180°, so $\Phi : 0^\circ \sim 90^\circ$. The intrinsic parameters of the simulated catadioptric camera are: $r = 1$, $s = 0$, $u_0 = 0$, $v_0 = 0$, and $f_e = 400$. We let the catadioptric camera with $l = 0.966$ as an example to illustrate the qualities of fitting catadioptric conics. Obviously, catadioptric conics from the catadioptric camera can belong to any type of conic, such as, ellipse, parabola, hyperbola, etc. Generally speaking, it is very difficult to extract a conic whose type is unknown from image with high accuracy. In order to simplify this problem, we only consider the case where the catadioptric conics are ellipses. It is well known that a conic is an ellipse when $ac - b^2 > 0$. From (10), we know that if a metric catadioptric conic of a space line is an ellipse, it must satisfy: $l^2 - 1 + n_z^2 > 0$. So, we obtain $0^\circ \le \Phi < 75.0164^\circ$. From (9), we know that if a metric catadioptric conic of a space sphere is an ellipse, it must satisfy: $(l^2 - 1)(1 - n_z^2) + (d_0 + l \cdot n_z)^2 > 0$. So, we obtain $0.2585 < d_0 \le 1$ for all Φ. We wish in this experiment to investigate the effects that occlusion and eccentricity of

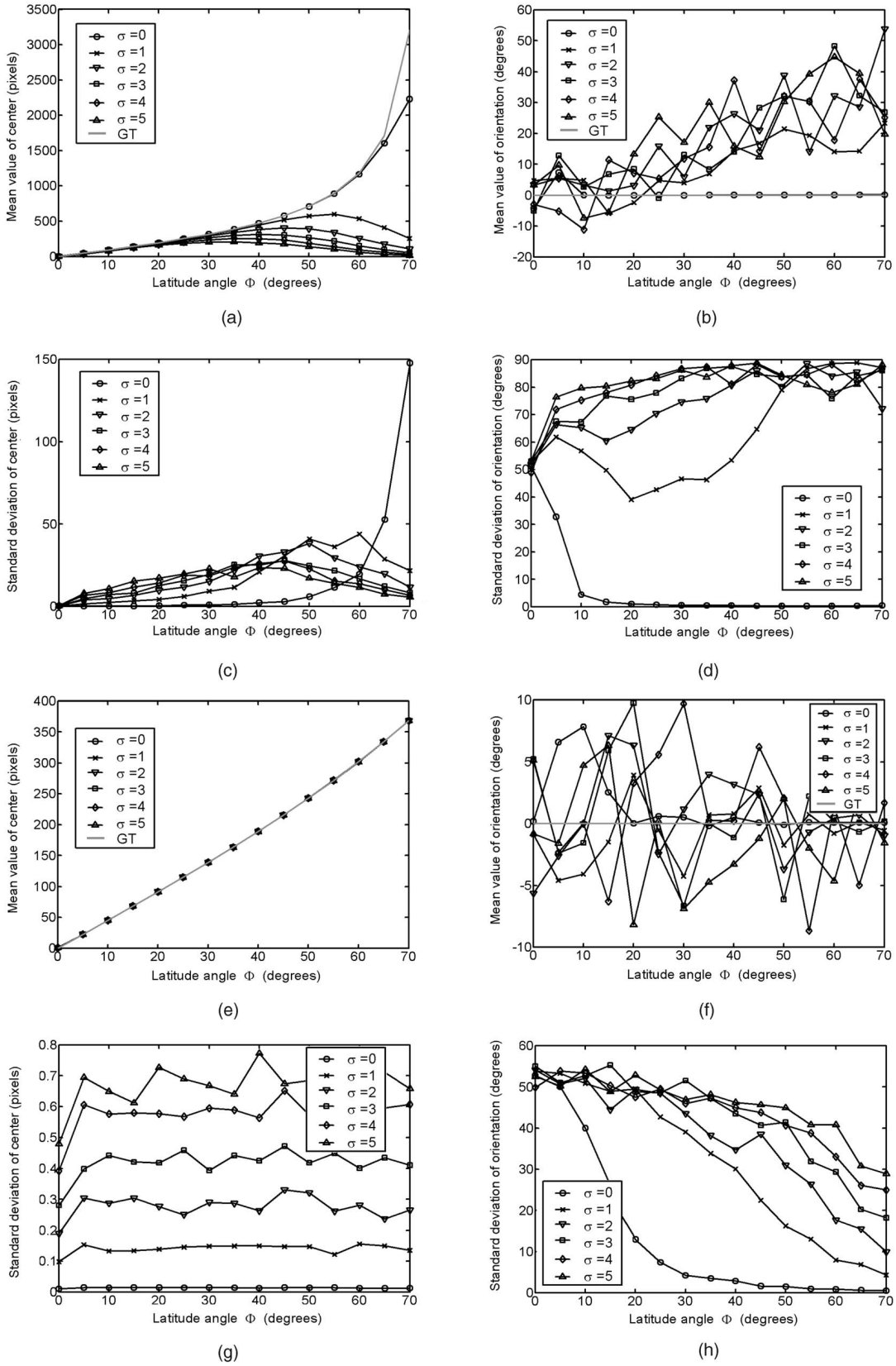

Fig. 3. The results of catadioptric conic fitting for line and sphere images. (a), (b), (c), and (d) for line images. (e), (f), (g), and (h) for sphere images. "GT" means "Ground Truth." See text for details.

the ellipse have on the fitting accuracy. Two simulated images containing the metric catadioptric conics of lines and spheres are shown in Fig. 2.

The ellipse parameters are expressed as a 5-vector $(c_x, c_y, R_x, R_y, \theta)$, where (c_x, c_y) is the ellipse center, R_x and R_y are the major and minor semi-axes, respectively, and

TABLE 4
Five Different Calibration Experiments for Comparison

	Method	Parameters			
		l	Φ	Θ	d_0
1	**IS**	0.966	$40° \sim 70°$	$0° \sim 360°$	$0.96 \sim 0.98$
2	**IL**	0.966	$0° \sim 30°$	$0° \sim 360°$	-
3	**PL**	0.966	$0° \sim 30°$	$0° \sim 360°$	-
4	**IS**	0.8	$40° \sim 70°$	$0° \sim 360°$	$0.96 \sim 0.98$
5	**IS**	0.966	$20° \sim 50°$	$0° \sim 360°$	$0.96 \sim 0.98$

θ is the counterclockwise angle in degrees between the major axis and the positive X axis. There are many conic fitting methods described in [28]. Here, a method presented in [9] for least squares fitting of ellipses is used. The method is rotation and translation invariant. That means using this method, the accuracy of ellipse fitting is independent of center and orientation of the ellipse. Therefore, we select $\Theta = 0°$ and $0° \leq \Phi \leq 70°$ for all lines and spheres, and $d_0 = 0.97$ for all spheres.

On each image ellipse we choose 100 points (or on a portion of an ellipse when it is the projection of a line, see Fig. 2a). Gaussian noise with zero-mean and σ standard deviation is added to these image points. The noise levels σ are 0, 1, 2, 3, 4, 5, respectively. For each noise level, we perform 1,000 independent trials, and the mean values and standard deviations of these recovered parameters are computed over each run. We found the estimated results for major semi-axis and minor semi-axis errors as the measures have no qualitative difference from those for center. The similar observation is also stated in [8]. Therefore, only the experiment results of center and orientation are shown in Fig. 3. Note that Barreto and Araújo [4] have studied the performances of fitting paracatadioptric projections of lines.

Finding 1: From Figs. 3a, 3b, 3c, and 3d, i.e., the results of catadioptric conic fitting for line images, we find that the mean values of center are degraded very fast with respect to Φ. The standard deviations of center first increase but then decrease with Φ. The mean values of orientation are very bad since the estimated orientations are different from the ground truth even about 90 degrees. The main reason for these is due to the effects of occlusion. With increasing Φ, the occluding partition increases (see Fig. 2a). For Φ near 70 degree, the curve approximates to a line segment, so the estimated center is very far from the ground truth. For $\Phi = 0$, the ellipse is a circle (i.e., the FOV boundary, see Fig. 2a), so the estimated orientations in this case are randomly distributed within $0° \sim 90°$.

Finding 2: From Figs. 3e, 3f, 3g, and 3h, i.e., the results of catadioptric conic fitting for sphere images, we find that the mean values and the ground truth of center almost overlap. From Fig. 3g, the standard deviations of center increase linearly with the noise level. We find Φ has relatively little effect on the accuracy of ellipse center estimation, i.e., the ellipse center error curves are relatively flat. The mean values of orientation are almost bounded within $\pm 10°$. The reason for these is the image conics for spheres with complete data. The standard deviations of orientation with small Φ are high but then decrease with increasing Φ. The reason for these is a conic with small Φ is very close to a circle and with small eccentricity, whereas the eccentricity would increase along with the increasing of Φ.

Comments: Fitting the catadioptric conics of spheres is more robust than those of lines. The experiments in [8] illustrate that the key parameters affecting the ellipse fitting algorithms' accuracy is the amount of occlusion and the qualitative noise level. With complete data, all ellipse fitting algorithms exhibit a similar degradation in the presence of increasing noise. From our experiments, we notice that the eccentricity of an ellipse is another key factor especially affecting the accuracy of orientation estimation.

5.2 Calibration with Simulated Data

In this section, we first compare **IS** with **IL** and **PL**, and then study the performances of **IS**. As we know the eccentricity of a catadioptric image conic of a line or a sphere in space is determined by parameter l and Φ. When $l \to 1$, or $\Phi \to 0°$, the image conic is close to a circle and has small eccentricity, and the accuracy of fitting an ellipse with small eccentricity is not high because of the low accuracy of estimated orientation. Therefore, we compare the calibration results based on **IS** with different parameters l, and also compare those with different Φ. There are five different calibration experiments for comparison as listed in Table 4.

The simulated catadioptric cameras have the following parameters: $r = 1$, $s = 0$, $u_0 = 500$, $v_0 = 500$, and $f_e = 400$. The parameter l for different catadioptric cameras is shown in Table 4. We generate two different kinds of images: the first contains the image conics of space spheres and the second contains the image conics of space lines. The variables Φ, Θ, and d_0 which are used to represent the 3D locations of these lines and spheres with respect to the camera are uniformly distributed within their valid ranges as shown in Table 4. The projection of the mirror boundary is also generated in each image. Since it is difficult to select a good fixed threshold due to lighting changing and non-uniformity of directional lighting, we only select about one-third of the entire ellipse of the boundary to simulate the actual conditions. The number of curves in each image is 4, 8, or 12, respectively. On each projection curve we choose 100 points. Gaussian noise with zero-mean and σ standard deviation is added to these image points. We vary the noise level σ from 0 to 5 pixels. The conic fitting algorithm presented in [9] is used here. For each noise level, we perform 1,000 independent trials, and the mean values and standard deviations of these recovered parameters are computed over each run. The estimated results of these experiments are shown in Fig. 4. Since the performance of u_0 and v_0 are very similar, we only show the estimated results for u_0.

Comparison 1: Sphere (Experiment 1) versus Line (Experiments 2 and 3) The estimated results of r, s', and f_e in Experiment 1 (**IS**) are better than those in Experiment 2 (**IL**). The estimated results of principal point in Experiment 1 are similar to those in Experiment 2. The estimated results of r, s', and principal point in Experiment 1 are better than those in Experiment 3 (**PL**). Note that the mean values of f_e in Experiments 1 and 3 are varied with respect to noise level in opposite directions. The main reason for all these may be

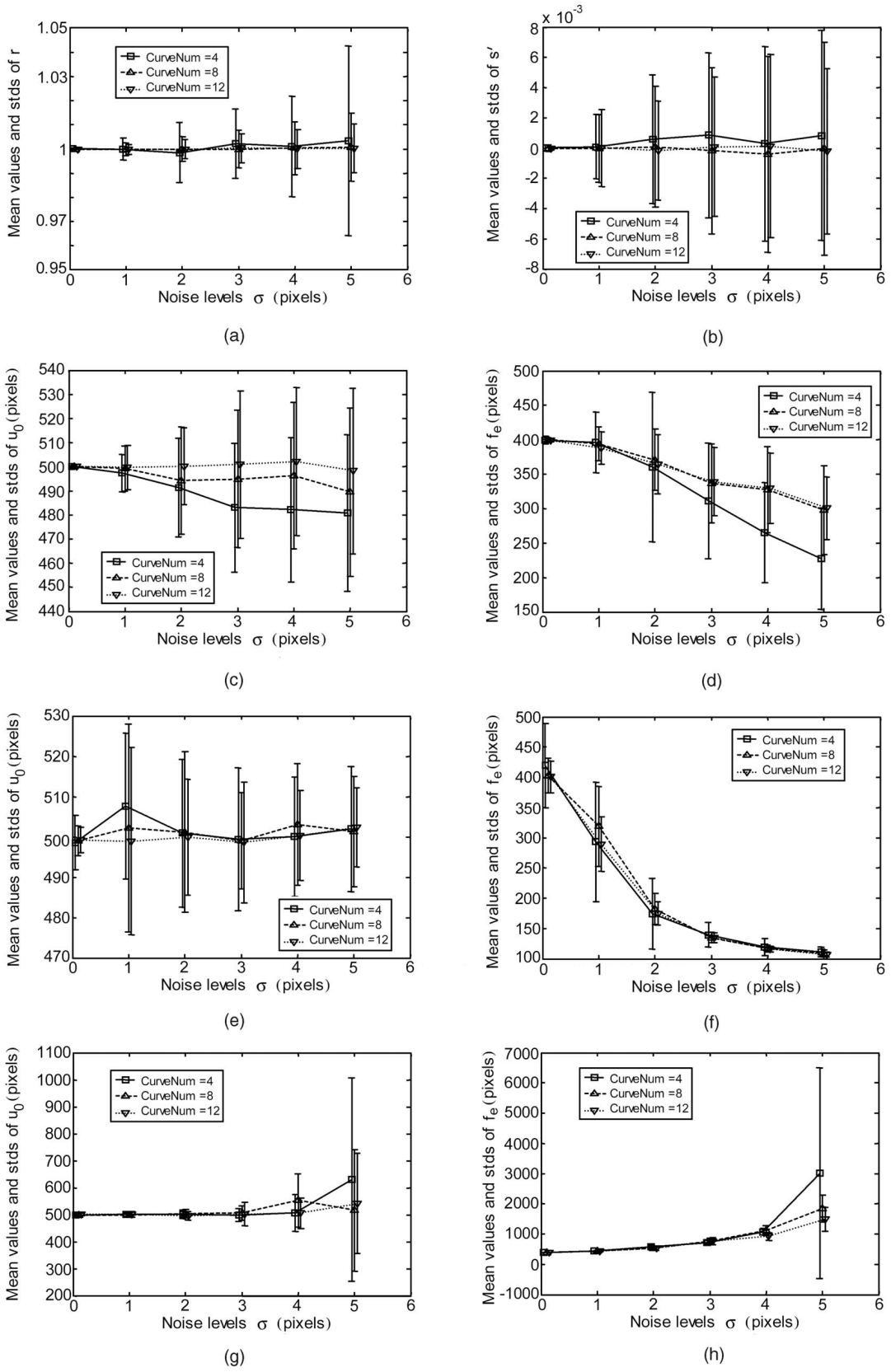

Fig. 4. The estimated results of simulated experiments. (a), (b), (c), and (d) for Experiment 1 in Table 4. (e) and (f) for Experiment 2, (g) and (h) for Experiment 3. See text for details.

owe to the different fitting accuracy for line and sphere images. Therefore, we obtain that calibrating catadioptric cameras using sphere images (**IS**) is better than those using line images (**IL** and **PL**).

(a) (b)

Fig. 5. Two examples of real images used in our experiments.

Comparison 2: $l = 0.966$ (Experiment 1) versus $l = 0.8$ (Experiment 4). The estimated results of principal point and f_e in Experiment 4 are better than those in Experiment 1, while the estimated results of r, s' in Experiment 4 are similar to those in Experiment 1. The main reason for these is the high accuracy of fitting ellipse with large eccentricity. Hence, for using **IS**, the calibration results from a catadioptric camera with small l are better than those with large l.

Comparison 3: $\Phi : 40^\circ \sim 70^\circ$ (Experiment 1) versus $\Phi : 20^\circ \sim 50^\circ$ (Experiment 5). The estimated results of f_e in Experiment 5 are worse than those in Experiment 1. The standard deviations of principal point in Experiment 5 are slightly worse than those in Experiment 1. Other estimations are very similar in Experiments 5 and 1. The main reason for these is similar to that in Comparison 2. Therefore, for using **IS**, the calibration results using spheres distributed near the edge of the FOV will be better than those near the middle.

5.3 Calibration with Real Data

The test sphere for the real image experiments is a billiard ball. The ball is placed in front of a white screen in order to create high contrast lighting environments. We take images of the ball using the catadioptric camera described before. A total of 10 sphere images are taken. For comparison purpose, 10 images containing line image are also taken. The experimental images are shown in Fig. 5. The resolution of these images is $2,048 \times 1,536$. Image conic extracting is accomplished by a software package developed by our lab. On each line image, only the conic with largest arc length is selected. In order to obtain unbiased results, these sphere images or line images should be uniformly distributed within the image. Among these 10 images (sphere images or line images), eight of them are selected as a group for calibration. Due to lack of the ground truth of calibration, we select FOV of the catadioptric camera as the estimation to evaluate the accuracy of the calibration results. The ground truth of FOV is 217.2 degree given by the producer. The calibration results with real data are listed in Table 5. The results of FOV show that the calibration results using sphere (**IS**) seem be more consistent with the ground truth of FOV than those using lines (**IL** and **PL**).

TABLE 5
Calibration Results with Real Data

Method	**IS**	**IL**	**PL**
r	1.0034 ± 0.0007	1.0043 ± 0.0006	1.012 ± 0.003
s'	$4.8\times10^{-4} \pm 0.4\times10^{-4}$	$6.2\times10^{-4} \pm 0.8\times10^{-4}$	0.0023 ± 0.0009
u_0	1054.8 ± 3.4	1052.1 ± 5.7	1048.6 ± 6.2
v_0	769.2 ± 3.7	774.3 ± 6.8	771.4 ± 5.4
f_e	507.8 ± 6.9	453.7 ± 23.6	543.1 ± 18.4
FOV	215.3 ± 2.2	228.5 ± 8.3	207.6 ± 6.5

6 Conclusions

In this paper, we present a unified framework for the calibration of central catadioptric cameras based on images of space lines or space spheres. We show that, in general, each line image has three invariants, whereas each sphere image has only two. Some degenerated configurations of invariants are also investigated, and the derivations seem to be consistent with those of planar and parabolic cases which have be derived by other researchers. These invariants are used to derive the constraint equations on the intrinsic parameters. A practical two-stage calibration technique, which divides the intrinsic parameters into two groups, is proposed in order to efficiently solve the nonlinear constraint equations for the intrinsic parameters. Extensive experiments on simulated or real data show that the sphere-based calibration generally and largely outperforms, in terms of both robustness and accuracy, that based on space lines, which are currently mostly used calibration entities. The underlying reason of such superiorities of spheres over lines seems primarily due to different errors in conic fitting process.

Appendix

Under metric paracatadioptric projection, a space line is projected into a circle $\mathbf{C_L}$:

$$ax^2 + ay^2 + 2dx + 2ey + f = 0. \tag{25}$$

The distance between the center of the circle O_L and the origin of image coordinate system O_P is denoted by $d_L = |O_L O_P|$ as shown in Fig. 6, and the radius of the circle is represented as r_L. From (25), we have:

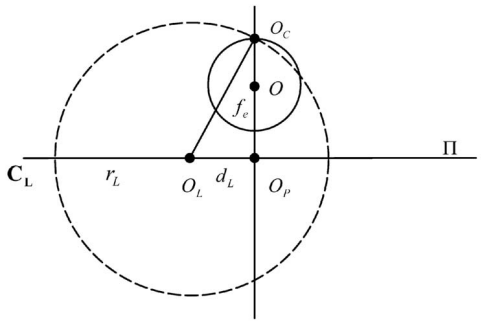

Fig. 6. A cross-section of the geometric interpretation of Invariant $f_e^2 = -f/a$. Some notations are the same as those used in Fig. 1. The solid circle represents the viewing sphere. The dashed circle represents the sphere constructed from the circle $\mathbf{C_L}$ where $\mathbf{C_L}$ is chosen as the equator of the sphere.

$$d_L^2 = \frac{d^2 + e^2}{a^2} \text{ and } r_L^2 = -\frac{f}{a} + \frac{d^2 + e^2}{a^2}. \quad (26)$$

From (26) and Invariant $f_e^2 = -\frac{f}{a}$, we obtain:

$$f_e^2 = r_L^2 - d_L^2.$$

This is Proposition 1 in [13]. Note that for paracatadioptric camera, the effective focal length in the generalized imaging model is twice the focal length used in [13].

ACKNOWLEDGMENTS

This work was supported by the National Key Basic Research and Development Program (973) under grant no. 2002CB312104 and the Natural Science Foundation of China under grant no. 60121302.

REFERENCES

[1] D. Aliaga, "Accurate Catadioptric Calibration for Real-Time Pose Estimation of Room-Size Environments," *Proc. Eighth Int'l Conf. Computer Vision,* vol. I, pp. 127-134, 2001.
[2] S. Baker and S. Nayar, "A Theory of Single-Viewpoint Catadioptric Image Formation," *Int'l J. Computer Vision,* vol. 35, no. 2, pp. 175-196, 1999.
[3] J. Barreto and H. Araújo, "Geometric Properties of Central Catadioptric Line Images," *Proc. Seventh European Conf. Computer Vision,* pp. 237-251, 2002.
[4] J. Barreto and H. Araújo, "Direct Least Square Fitting of Paracatadioptric Line Images," *Proc. IEEE. Conf. Computer Vision and Pattern Recognition Workshop Omnidirectional Vision and Camera Networks,* vol. VII, p. 78, 2003.
[5] S. Bogner, "Introduction to Panoramic Imaging," *Proc. IEEE Int'l Conf. Systems Man and Cybernetics,* pp. 3100-3106, 1995.
[6] D. Brown, "Close Range Camera Calibration," *Photogrammetric Eng.,* vol. 37, no. 8, pp. 855-866, 1971.
[7] N. Daucher, M. Dhome, and J. Lapresté, "Camera Calibration from Spheres Images," *Proc. Third European Conf. Computer Vision,* pp. 449-454, 1994.
[8] A. Fitzgibbon and R. Fisher, "A Buyer's Guide to Conic Fitting," *Proc. Sixth British Machine Vision Conf.,* pp. 513-522, 1995.
[9] A. Fitzgibbon, M. Pilu, and R. Fisher, "Direct Least Square Fitting of Ellipses," *IEEE Trans. Pattern Analysis and Machine Intelligence,* vol. 21, no. 5, pp. 476-480, May 1999.
[10] C. Geyer and K. Daniilidis, "Catadioptric Camera Calibration," *Proc. Seventh Int'l Conf. Computer Vision,* vol. I, pp. 398-404, 1999.
[11] C. Geyer and K. Daniilidis, "Catadioptric Projective Geometry," *Int'l J. Computer Vision,* vol. 45, no. 3, pp. 223-243, 2001.
[12] C. Geyer and K. Daniilidis, "Structure and Motion from Uncalibrated Catadioptric Views," *Proc. IEEE. Conf. Computer Vision and Pattern Recognition,* vol. I, pp. 279-286, 2001.
[13] C. Geyer and K. Daniilidis, "Paracatadioptric Camera Calibration," *IEEE Trans. Pattern Analysis and Machine Intelligence,* vol. 24, no. 5, pp. 687-695, May 2002.
[14] M. Grossberg and S. Nayar, "A General Imaging Model and a Method for Finding its Parameters," *Proc. Eighth Int'l Conf. Computer Vision,* vol. II, pp. 108-115, 2001.
[15] J. Hong, X. Tan, R. Weiss, and E. Riseman, "Image-Based Homing," *Proc. IEEE. Conf. Robotics and Automation,* pp. 620-625, 1991.
[16] S. Kang, "Catadioptric Self-Calibration," *Proc. IEEE. Conf. Computer Vision and Pattern Recognition,* vol. I, pp. 201-207, 2000.
[17] V. Nalwa, "A True Omnidirectional Viewer," technical report, Bell Labs, Holmdel, 1996.
[18] S. Nene and S. Nayar, "Stereo with Mirrors," *Proc. Sixth Int'l Conf. Computer Vision,* pp. 1087-1094, 1998.
[19] T. Pajdla, T. Svoboda, and V. Hlavac, "Epipolar Geometry of Central Panoramic Cameras," *Panoramic Vision: Sensors, Theory, and Applications,* R. Benosman and S.B. Kang, eds., pp. 85-114, 2001.
[20] M. Penna, "Camera Calibration: A Quick and Easy Way to Determine the Scale Factor," *IEEE Trans. Pattern Analysis and Machine Intelligence,* vol. 13, no. 12, pp. 1240-1245, Dec. 1991.
[21] L. Quan, "Conic Reconstruction and Correspondence from Two Views," *IEEE Trans. Pattern Analysis and Machine Intelligence,* vol. 18, no. 2, pp. 151-160, Feb. 1996.
[22] J. Semple and G. Kneebone, *Algebraic Projective Geometry.* Oxford Science, 1952.
[23] G. Stein, "Internal Camera Calibration Using Rotation and Geometric Shapes," master's thesis, Artificial Intelligence Lab, MIT, 1993.
[24] T. Svoboda, T. Padjla, and V. Hlavac, "Epipolar Geometry for Panoramic Cameras," *Int'l J. Computer Vision,* vol. 49, no. 1, pp. 23-37, 2002.
[25] R. Swaminathan and S. Nayar, "Non-Metric Calibration of Wide-Angle Lenses and Polycameras," *IEEE Trans. Pattern Analysis and Machine Intelligence,* vol. 22, no. 10, pp. 1172-1178, Oct. 2000.
[26] R. Swaminathan, M. Grossberg, and S. Nayar, "Caustics of Catadioptric Camera," *Proc. Eighth Int'l Conf. Computer Vision,* vol. II, pp. 2-9, 2001.
[27] Y. Yagi and S. Kawato, "Panorama Scene Analysis with Conic Projection," *Proc. IEEE Workshop Intelligent Robots and Systems,* pp. 181-187, 1990.
[28] Z. Zhang, "Parameter Estimation Techniques: A Tutorial with Application to Conic Fitting," *Image and Vision Computing,* vol. 15, no. 1, pp. 59-76, 1997.

Xianghua Ying received the BS degree in computer science from North China Electric Power University in 1997, and the MS degree in astronomical instrument from the National Astronomical Observatories at the Chinese Academy of Sciences, Beijing, China, in 2001. Currently, he is pursuing the PhD degree in the National Laboratory of Pattern Recognition at the Institute of Automation Chinese Academy of Sciences, Beijing, China. His current research interests include computer vision, computer graphics, robot navigation, and image processing.

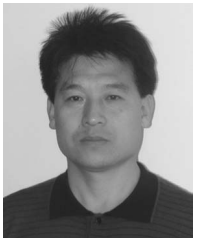

Zhanyi Hu received the BS degree in automation from the North China University of Technology in 1985 and the PhD degree (Docteur d'Etat) in computer science from the University of Liege, Belgium, in 1993. Since 1993, he has been with the Institute of Automation at the Chinese Academy of Sciences. From May 1997 to May 1998, he also was a visiting scholar at the Chinese University of Hong Kong. He now is a research professor of computer vision, a member of the Executive Expert Committee of the Chinese National High Technology R&D Program, and an associate editor for *Journal of Computer Science and Technology* and the *Chinese Journal of CAD and CG*. His current research interests are in robot vision, which include camera calibration, 3D reconstruction, active vision, geometric primitive extraction, vision guided robot navigation. He has published more than 60 peer-reviewed papers on major national and international journals.